

## Friction in clay-bearing faults increases with the ionic radius of interlayer cations

Hiroshi Sakuma<sup>1</sup><sup>✉</sup>, David A. Lockner<sup>2</sup><sup>✉</sup>, John Solum<sup>3</sup> & Nicholas C. Davatzes<sup>4</sup>

Smectite can dramatically reduce the strength of crustal faults and may cause creep on natural faults without great earthquakes; however, the frictional mechanism remains unexplained. Here, our shear experiments reveal systematic increase in shear strength with the increase of the ionic radius of interlayer cations among lithium-, sodium-, potassium-, rubidium-, and cesium-montmorillonites, a smectite commonly found in faults. Using density-functional-theory calculations, we find that relatively small sodium ions fit in the ditrigonal cavities on the montmorillonite surfaces, resulting in weakening of interlayer repulsion during sliding. On the other hand, relatively large potassium ions do not fit in the ditrigonal cavities, resulting in a larger resistance to sliding due to electrostatic repulsion between potassium ions. Calculated shear strength is consistent with our shear experiments by considering the partial dehydration of the frictional contact area. These results provide the basis for developing a quantitative model of smectite-bearing fault rheology.

<sup>1</sup>Functional Clay Materials Group, National Institute for Materials Science, Tsukuba 3050044, Japan. <sup>2</sup>U.S. Geological Survey, Menlo Park, California, CA 94025, USA. <sup>3</sup>Carbonate Research, Integrated Geoscience Department, Shell Global Solutions International B.V., Kesslerpark 1, 2288 GS Rijswijk, ZH, The Netherlands. <sup>4</sup>Department of Earth and Environmental Science, Temple University, Philadelphia, PA 19122, USA. ✉email: [SAKUMA.Hiroshi@nims.go.jp](mailto:SAKUMA.Hiroshi@nims.go.jp); [dlockner@usgs.gov](mailto:dlockner@usgs.gov)

The central creeping portion of the San Andreas Fault deforms without great earthquakes<sup>1</sup>. Unexpectedly large slip occurred near the Japan trench during the 2011 Tohoku-oki earthquake, which in turn caused the launch of a huge tsunami. These phenomena of fault creep and very large fault slip suggest low fault strength that is, in part, attributed to the presence of weak clay minerals<sup>2–6</sup>. The shear strength of smectite is unique in clay minerals, because the friction coefficient dramatically changes from dry to wet<sup>7–9</sup> as shown in Fig. 1 for Na-montmorillonite (Na-Mnt) which is a common smectite clay. The shear strength increases with increasing confining pressure (burial depth)<sup>8</sup> and is dependent on the type of exchangeable cations<sup>9–11</sup>. Smectite has a layered crystal structure with a net negative charge that is neutralized by weakly bound interlayer and surface cations. Additionally, the charge imbalance can cause crystals to swell by taking up interlayer water as well as forming layers of structured water on exterior surfaces, acting as a lubricant, and reducing shear strength by as much as 80%<sup>8</sup>. A central question is to what degree the interlayer water is stable to act as a lubricant at depth.

X-ray diffraction and thermal analysis have revealed that Mnt hydrates with two or three molecular layers of interlayer water under crustal pressures<sup>12–15</sup>. These few layers of water around the surface cations apparently act as a good lubricant as revealed by surface force measurements on mica<sup>16–19</sup>. These observations imply that the friction coefficient of wet Mnts is low, independent of the species of interlayer surface cations. However, previous shear experiments revealed a clear difference in the shear strength between wet Na- and K-Mnts<sup>11</sup>.

To reveal the effect of cationic species, we hypothesize that stress concentrations can occur on the sliding contact area, leading to local loss of lubrication. If this is correct, the difference in the friction coefficient of wet Na- and K-Mnts should be associated with a difference in the friction coefficient of the dehydrated states. The shear strength of wet cation-exchanged Mnt gouges is measured by triaxial shear experiments and we confirm the clear difference in the shear strength among Li-, Na-, K-, Rb-, and Cs-Mnts. To interpret the interlayer-cation influence on friction, we conducted atomic-scale shear simulations on dry Na- and K-Mnts using density functional theory (DFT). The simulations support the hypothesis of the local loss of water lubrication on the sliding contact area.

## Results and discussion

**Deformation tests of wet montmorillonite.** We present a suite of triaxial deformation experiments conducted at a constant effective normal stress of 40 MPa on a commercial Na-montmorillonite clay. By using a standard washing procedure, the weakly bound Na<sup>+</sup> cations were exchanged for Li<sup>+</sup>, K<sup>+</sup>, Rb<sup>+</sup> and Cs<sup>+</sup> to provide five starting materials. Shearing experiments reveal the influence of bulk water chemistry and exchangeable cations on the shear strength of montmorillonite (Fig. 1). Consistent with earlier studies<sup>8</sup>, the addition of water to dry Mnt has a profound influence in reducing the coefficient of friction  $\mu$  (defined as the ratio: (shear stress)/(normal stress – pore pressure)). This effect is demonstrated in Fig. 1 by the difference between dry and distilled (DW) water-saturated Na-Mnt. A second effect shown in the figure is that increasing brine concentration results in increasing coefficient of friction. The addition of 1 M<sub>aq</sub> of both NaCl and KCl salt solutions increases  $\mu$  by approximately 0.02 (similar to results reported in a previous study<sup>11</sup>). This difference between DW and brine can be interpreted by the difference in swelling pressure of Mnt which decreases with increasing salinity<sup>20</sup>. The high swelling (disjoining) pressure expands the interlayer distance of Mnt by the

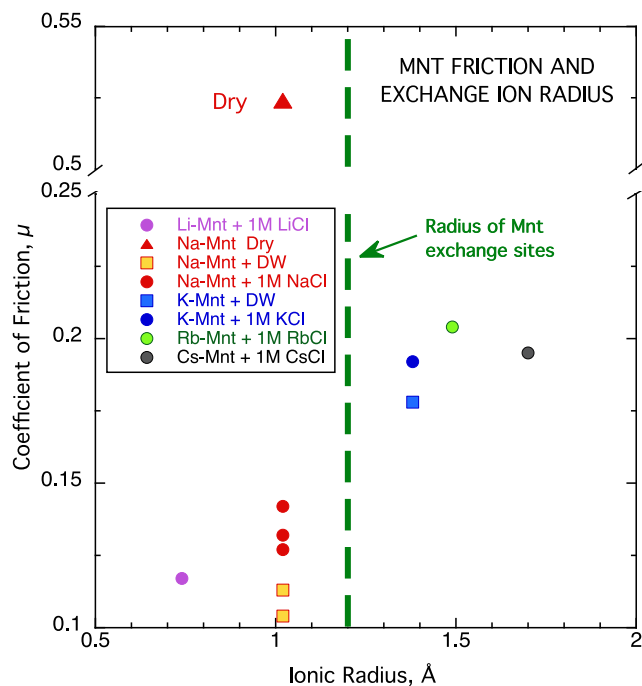


**Fig. 1 Friction coefficient of Li-, Na-, K-, Rb-, and Cs-montmorillonites (Mnt) under dry and wet conditions.** Friction coefficients are measured by triaxial shear experiments at effective normal stress of 40 MPa, both dry and wet, by adding distilled water (DW) or brine (1 M salts). Horizontal axis indicates the ionic radii of interlayer cations determined from six-coordinated anions<sup>46</sup>. A vertical dashed line indicates the radius of the cavity (2.6 Å)<sup>47</sup> minus the ionic radius of six-coordinated oxygen ions (1.4 Å)<sup>46</sup>. In the DFT calculations, the size of the cavity was relaxed to be stable depending on the cationic species, but there is no clear difference between Na- and K-Mnts in the radius of the average cavity (2.6 Å).

intercalation of water and enhances the water lubrication. This pressure also reduces the effective normal stress (normal stress minus pore pressure) within the clay structure, rendering the low friction in DW. The strength difference between Na-Mnt in DW and in brine (Fig. 1) gives a rough estimate of swelling pressure of ~7.5 MPa (see comment in Supplementary Discussion, Triaxial Deformation Experiments), comparable with reported values between 5–10 MPa<sup>20</sup> (using the dry density of 1974 kg m<sup>-3</sup> for our samples). A third strength effect is observed when interlayer and surface exchange cations are replaced. A systematic increase in  $\mu$  occurs as monovalent cationic radius increases from Li<sup>+</sup> to Cs<sup>+</sup> under wet conditions (Fig. 1).

**Montmorillonite structure.** Montmorillonite is a 2:1 sheet silicate in which a central octahedral sheet is sandwiched between two silicon-oxygen tetrahedral sheets (Fig. 2a). In-plane bonds are stronger than inter-plane bonds, leading to a pronounced basal cleavage. Substitutions in either tetrahedral or octahedral sheets can lead to a net negative charge that attracts weakly bound cations to exchange sites on the tetrahedral surfaces. In addition to providing sites for the interlayer cations, weak bonding between adjacent tetrahedral layers can accommodate up to 3 layers of water (approximately 15 weight percent) and thus the moniker of swelling clay. The interlayer water and accompanying solvated ions are structured and energetically favored by reducing bonding forces between tetrahedral sheets. One consequence is that they reduce the resistance to basal shear.

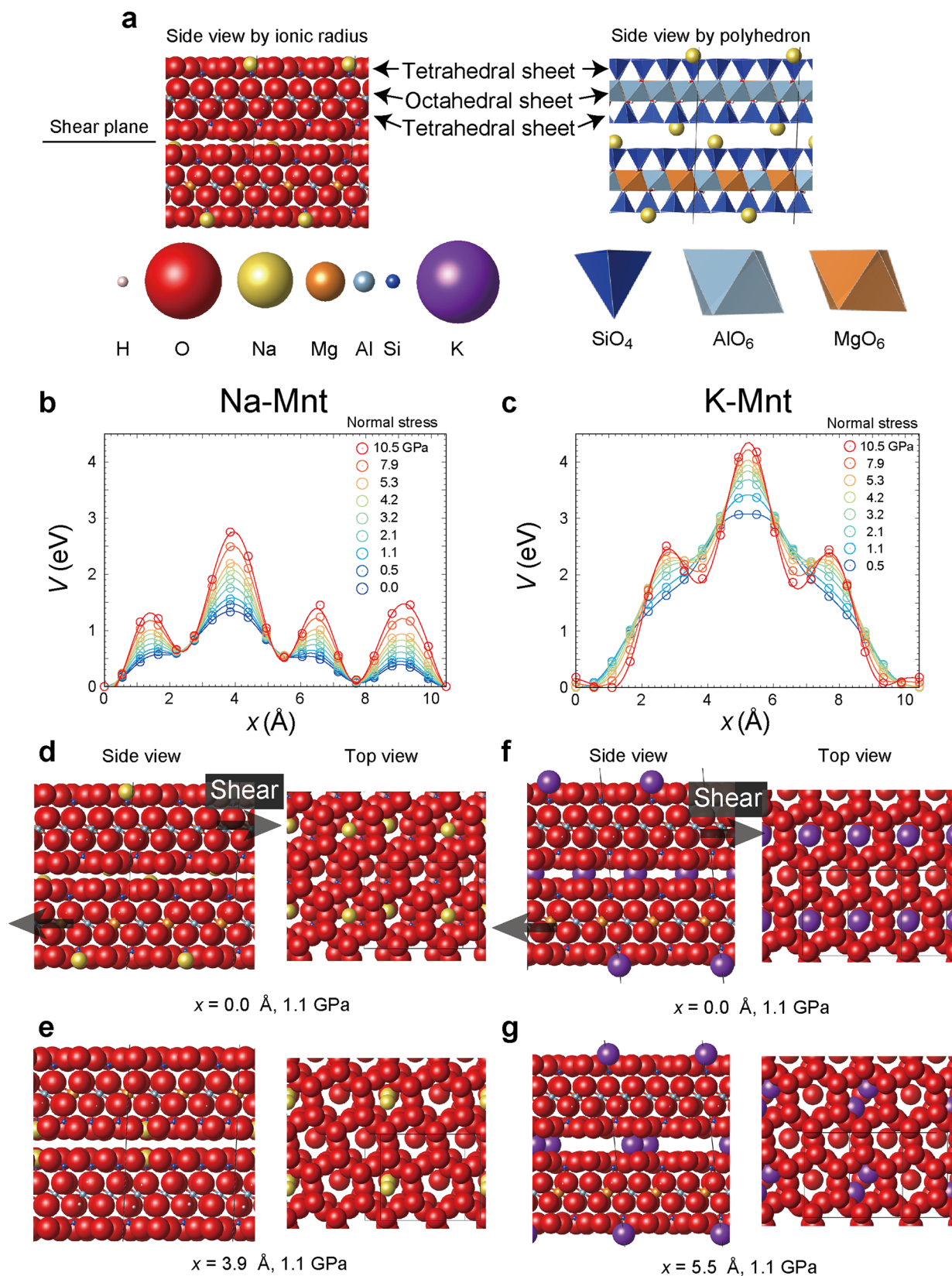


**Fig. 2** Potential energy changes along [100] sliding path for montmorillonites. **a** Structure of Mnt shown by ionic radius and polyhedron. The tetrahedral sheet is composed of SiO<sub>4</sub> tetrahedra and the octahedral sheet is composed of AlO<sub>6</sub> and MgO<sub>6</sub> octahedra. Potential energy changes for Na-Mnt (**b**) and K-Mnt (**c**). Structures in the most stable stacking state ( $x = 0$  Å) (**d** and **f**) are modified by the ionic size of interlayer cations as shown in top views. Maximum potential energy is characterized by overlapping of interlayer cations for Na-Mnt at  $x = 3.9$  Å (**e**) and for K-Mnt at  $x = 5.5$  Å (**g**).

The 2:1 structure of Mnt means that exterior basal surfaces are all tetrahedral sheets with the same properties as the interlayer tetrahedral sheets. Exterior surfaces have the same exchange sites and spontaneously form structured water layers when wet. For clay-filled faults in the mid to upper crust, effective normal stress is sufficient to force adjacent clay platelets close together, so that there is little difference between the interlayer and exterior water or interlayer and exterior exchange cations. This will be true for the mechanical shearing forces within a clay crystal as well as between adjacent clay crystals. For the remainder of this paper we will not make a distinction between interlayer shearing and shearing between crystals.

**DFT calculations for dry montmorillonite.** When considering the shear strength of clay-filled crustal faults, appropriate conditions will, in nearly all cases, be water- or brine-saturated. However, at this point, DFT calculations of water-saturated clay are not feasible and we are limited to calculations of dry Mnt with charge balance achieved by adding exchange cations. A direct comparison would imply conducting laboratory tests under dry conditions as well. However, the shear strength of Mnt is highly sensitive to water content<sup>7–9</sup>, where even a single monolayer of adsorbed or interlayer water will affect shear strength. Given the hydrophilic nature of Mnt, it is difficult to prepare nominally dry samples with consistent trace levels of moisture. In addition, the friction of dry Mnt is high enough to activate more shear mechanisms than simple basal slip, including rolling, jamming on face-edge contacts, Coulomb-style dilatancy, the comminution of grains, and probably more such as a recent study on the resistance of overlapping grain edges<sup>21</sup>. The basal slip mechanism is likely to be masked in dry gouge deformation. Since the expected differences in strength between our clay samples are small, we did not attempt to perform experiments to compare dry strengths. Instead, the tests with the best reproducibility and most direct bearing on natural fault conditions were precisely controlled pore pressure experiments that maintained full saturation. Furthermore, delamination of smectite layers is expected in wet experiments due to swelling and the preferred orientation for shearing may occur at grain-grain contacts. This increases the relative contribution to the friction of basal slip compared to face-edge contacts in wet Mnt.

We now present DFT calculations of shearing of dry Na- and K-Mnt to test our hypothesis of the local loss of water lubrication on the frictional contact area. Assuming that most slip occurs on the basal plane of layered clay minerals at wet conditions (without excessive misoriented particles to prevent basal slip), the friction of clays on the basal plane can be explained by the resistance to climb the barrier of the potential energy surface at contact areas during sliding<sup>22</sup>. The potential energy is the sum of the interlayer energy and the required work to move the layer against the normal force<sup>23</sup>. The interlayer energy is the repulsive or attractive energy at a given separation distance between two Mnt layers that results from the electrostatic and dispersion energies among atoms in the Mnts. The interlayer energy was calculated based on the dispersion-force corrected DFT by relaxing the atomic coordinates along sliding paths. The interlayer energies of clays are well determined by this method<sup>24</sup>.

Here we modeled two sliding paths by considering the distribution of interlayer cations. The definition of crystal axes follows that of  $2M_1$  muscovite because the structural model was built from muscovite. Friction can be expected to be independent of the crystallographic directions if there is no interlayer cation as for pyrophyllite<sup>25</sup>. Therefore, the difference in friction can be interpreted according to the difference in the distribution of interlayer cations. Slip in the [100] direction requires overlapping of

interlayer cations while slip in the [010] direction can occur without overlapping. Calculated potential energies along the [100] direction show some maxima for both Na- and K-Mnts (Fig. 2b, c). The shape is altered by exchanging the interlayer Na ions to K ions, even though the valence and number density are the same.

The valence states of these ions in Mnts are analyzed by the projected density of states (PDOS) of bulk Na- and K-Mnts (Supplementary Fig. 1). The highest occupied electrons are mainly characterized by the *p* orbital of O. There is a gap of 5 eV between the highest occupied and lowest unoccupied electronic levels and the unoccupied electronic level is characterized by the *s* orbital of Na or K ions. There is no difference in the electronic levels between Na- and K-Mnts. The partial charge of Na (+0.899) and K (+0.895) ions estimated by the Bader charge analysis<sup>26</sup> indicates that the electronegativity of Na ion is similar to that of K ion. A difference in the Na and K ions in the Bader analysis is the minimum distance to a surface on which the charge density is a minimum perpendicular to the surface. This distance of Na (1.82 Å) and K (2.46 Å) may be used for roughly estimating the difference in the size of ions. The size ratio K/Na is 1.35 which is consistent with that of effective ionic radius (Shannon and Prewitt, 1969),  $1.38/1.02 = 1.35$ .

From the above analysis of the electronic level and the charge density of Na<sup>+</sup> and K<sup>+</sup> ions, the difference in the potential energy profiles is mainly explained by the difference in ionic radii of Na<sup>+</sup> and K<sup>+</sup> ions. Principal cation exchange sites are the ditrigonal cavities (radius ~1.2 Å) of silicate sheets of Mnt. For most stable stacking structures at the sliding distance of  $x = 0$  Å, the smaller Na<sup>+</sup> ions can fit into these cavities (Fig. 2d). In an interlayer space, half of Na<sup>+</sup> ions strongly interact with the top layer and the other half interact with the bottom layer. This reduces the interaction between adjacent layers (Fig. 2d, e). By contrast, large K<sup>+</sup> ions cannot fit in the ditrigonal cavities and protrude from the layer resulting in strong interaction with both top and bottom layers (Fig. 2f). The maximum in the potential energy profiles increases with increasing normal stress, and the high potential energy is generated by the strong repulsion between interlayer cations (Fig. 2g). In Na-Mnts, Na<sup>+</sup> ions can fit in one of the nearest layers, while the large energy barrier (resistance to shear) in the K-Mnts is generated by the large repulsion between the protruding K<sup>+</sup> ions. The geometrical effect resulting from the size of interlayer ions compared to the ditrigonal cavity of Mnts determines the height of the potential energy barrier during sliding.

By contrast, the potential energy barrier along the [010] direction is relatively small for both Na- and K-Mnts as shown in Supplementary Fig. 2, because there is no overlapping of interlayer cations for this sliding path. It should be noted that the overlapping of interlayer cations solely depends on the distribution of interlayer cations. Therefore, the difference in the potential energy barrier between two crystallographic directions depends on the distribution of interlayer cations. In our model, the overlapping occurs along the [100] direction but this does not indicate that the crystallographic direction results in a high potential energy barrier in more disordered real systems.

Shear stress is calculated by the spatial derivative of potential energy as Eq. 5. The averaged shear stress was calculated along these sliding paths from the initial point through the symmetrically equivalent point. The shear stress of K-Mnt is larger than that of Na-Mnt when the overlapping of interlayer cations occurs such as in the [100] direction in our simulation model (Fig. 3a). If the overlapping of interlayer cations does not occur, as in the [010] direction in our model, the shear stress is smaller than that along the [100] direction and the difference between Na- and K-Mnts is small.

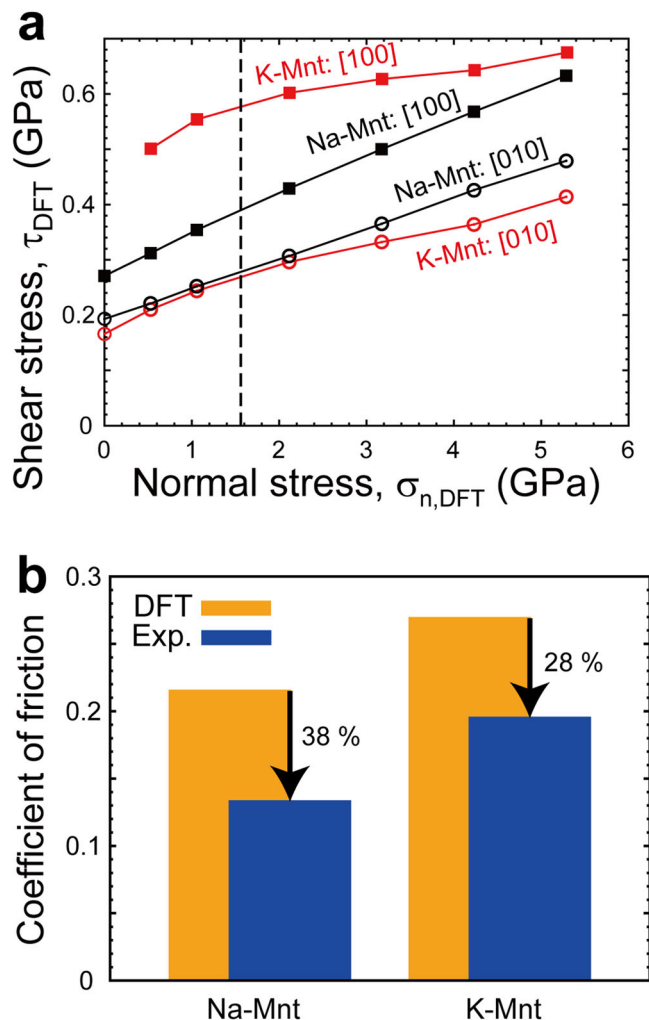


**Fig. 3 Comparison of the calculated dry friction with the wet shear experiments.** **a** Calculated shear stress for dry (dehydrated) real area of contact along [100] and [010] directions. The dashed line indicates the experimental indentation hardness of Mnt<sup>28</sup>. The shear stress of K-Mnt: [100] at zero normal stress cannot be calculated because the interlayer distance  $z$  determined from the balance between applied normal load and repulsive interlayer force cannot be estimated at some displacements, owing to the strong repulsion between top and bottom layers. The coefficients of friction of DFT study are averaged values of [100] and [010] directions at the normal stress of the dashed line. **b** Comparison of the calculated coefficient of dry friction with experimental coefficients of wet friction. The experimental values are obtained for brine-saturated Mnts at effective normal stress of 40 MPa.

The slightly larger shear stress of Na-Mnt compared to the K-Mnt along the [010] direction can be interpreted as the difference in the stacking structures of top and bottom tetrahedral sheets during the sliding. The shear stress depends on the total potential barrier to be climbed. The potential energy profile of Na-Mnt (Supplementary Fig. 2a) has two maxima at  $x = 2.6$  and  $7.5$  Å and shear stress is required to climb these two potential barriers. This shear stress is larger than that of the potential barrier of K-Mnt at  $x = 1-4.6$  Å (Supplementary Fig. 2b). This comparison indicates that the presence of a local potential minimum of Na-Mnt at  $x = 4-6$  Å creates the potential barrier at  $x = 6-7.5$  Å, resulting in high shear stress. The interfacial tetrahedra in aluminosilicate layers energetically avoid overlapping as discussed in pyrophyllite<sup>25</sup>. When interlayer cations are present, the overlapping changes to stabilize the interlayer

cations. The relatively large K ion requires the overlapping of interfacial ditrigonal cavities at  $x = 0$  Å, while the small Na ion can avoid overlapping (Supplementary Fig. 3). The stacking structure of Na-Mnt and K-Mnt at  $x = 4.8$  Å is quite different. The Na ion can be meta-stable in the ditrigonal cavities of top and bottom sheets, while the K ion is located on only one side of the ditrigonal cavity and this configuration is energetically unfavorable for K ions. This difference generates the difference in the potential energy profiles and shear stress.

**Implications for the difference in wet friction among cation exchanged Mnts.** Assuming that the normal stress at the real area of contact is equal to the indentation hardness of materials<sup>27</sup>, the shear stresses of Na- and K-Mnts along the [100] direction are estimated to be 0.39 and 0.57 GPa, and those along the [010] direction are 0.28 and 0.27 GPa (Fig. 3a). This calculation uses the experimental indentation hardness (1.56 GPa) of Na-montmorillonite<sup>28</sup>. The average coefficients of friction of Na- and K-Mnts can be estimated to be 0.22 and 0.27. The difference between Na- and K-Mnts is similar to that of brine-saturated experimental values (Fig. 3b).

Our simulations indicate that interlayer cations larger than the ditrigonal cavity exchange sites of the Mnt surface increase the shear resistance of dry montmorillonite. This may also explain the change in the strength of cation-exchanged wet montmorillonite observed in shear experiments and supports our hypothesis that stress concentrations can occur on the sliding contact area, leading to local loss of water lubrication. Dehydration by normal stress will occur above 1 GPa on the real area of contact of mica<sup>29</sup>. Such elevated normal stress will be achieved at portions of the real area of contact in wet montmorillonite even at the low applied effective normal stress of 40 MPa because the mean contact stress at real contact can be 100 times higher than the effective normal stress<sup>27</sup>. This also implies that such local loss of water lubrication can be expected at the effective normal stress higher than 10 MPa. This is consistent with the increase of the coefficient of friction of wet Na-Mnt with increasing the effective normal stress from 10 to 600 MPa<sup>8</sup>. We suggest that the dehydrated area of Na-Mnt may be smaller than that of K-Mnt because the decrease in the coefficient of friction from dry to wet Na-Mnt (38%) is larger than that of K-Mnt (28%) (Fig. 3b). This may be explained by the large hydration energy of the Na ion compared to the K ion<sup>30</sup>.

Here the role of interlayer water and surface-bound water at grain-grain contacts should be discussed. Two types of grain-grain contacts can be considered for the crystal structure of Mnt. One is the parallel contact of basal planes (face-face contact) that is similar to the interlayer space. This face-face contact becomes more like hydrated interlayer space as increasing normal stress expels all but the most strongly constrained 1 to 2 water layers; identified as the origin of the repulsive hydration force between micas<sup>31</sup>. The second type of contact is face-edge. The edge should be hydroxylated and therefore is hydrophilic. However, the attractive interaction with water should be smaller than that in the interlayer because of the lack of interlayer cations on the surface. The thickness of the water layer on the face-edge contacts is therefore expected to be thinner than the face-face contact and the friction on the face-edge contacts should be high. However, these face-edge contacts tend to be removed by shearing where the delamination of smectite layers in wet conditions favors the development of face-face contacts. Thus, both the basal slip friction at grain-grain contacts and at interlayers is important for wet friction of Mnt. The role of interlayer friction is evident from a comparison with the powder friction of non-swelling mica<sup>32,33</sup>.

Can interlayer slip occur in dry friction by providing a weak plane of uniform contact that shears coherently? From our dry DFT simulations, the shear stress at the real area of contact has a cohesion term  $c$  that is the zero normal stress intercept in Fig. 3a ( $c = 0.28$  GPa for Na-Mnt sheared in the [100] direction). The macroscopic shear stress can be described by using the shear stress  $\tau_{\text{DFT}}$  at the real area of contact  $A_r$  as

$$\begin{aligned}\tau_{\text{macro}} &= \frac{A_r}{A} \tau_{\text{DFT}} \\ &= \mu_{\text{DFT}} \sigma_{\text{macro}} + \frac{A_r}{A} c.\end{aligned}\quad (1)$$

Here,  $A$  is the nominal area of contact,  $\mu_{\text{DFT}}$  is the internal friction coefficient at  $A_r$  and  $\sigma_{\text{macro}}$  is the nominal normal stress. This equation indicates that macroscopic shear stress increases with increasing the real area of contact. The real area of contact for uniform deformation should be much larger than for rough grain-grain contacts, resulting in a larger contribution of cohesion to the overall shear strength. This result implies that the weaker grain-grain contacts will provide the dominant deformation mechanism under dry conditions.

The findings presented here should provide a starting point to develop a quantitative model of weak fault rheology at depth. For example, water lubrication in wet montmorillonite is expected at depth from the presence of interlayer and surface water in montmorillonite<sup>12–15,34</sup>. However, our results indicate that in addition, partial dehydration of the real area of shear contact can occur due to increased local normal stress associated with large adsorbed cations. This will result in an increase of shear strength beyond the estimation of stability of interlayer water based only on the average interlayer water thickness of montmorillonite. The clear difference in the shear strength between dry Na- and K-Mnts is important for fault shear strength at shallow depths where hydrated montmorillonites are common and at depth because ion exchange from Na to K is required for the smectite-illite transition found in sedimentary rocks<sup>35</sup>.

## Methods

**Potential energy and frictional force.** Macroscopic friction can be derived theoretically based on the atomic-scale friction<sup>22</sup>. Friction force in the atomic scale can be calculated if the potential energy along the sliding path is precisely determined<sup>23,36</sup>. The potential energy of clays has been estimated from the density functional theory (DFT) with a van der Waals correction<sup>22,25,37</sup>. The potential energy  $V$  is a function of interlayer energy  $E_{\text{IL}}$  and work to change the interlayer distance under the applied normal load  $f_{\text{ext}}$  according to

$$V(x; f_{\text{ext}}) = E_{\text{IL}}(x, z) + f_{\text{ext}}z. \quad (2)$$

Here,  $x$  is the sliding distance along the sliding path and  $z$  is the interlayer distance.

The interlayer energy  $E_{\text{IL}}$  was calculated from the DFT by:

$$E_{\text{IL}}(x, z) = E_{2\text{layers}}(x, z) - 2E_{1\text{layer}}. \quad (3)$$

Here,  $E_{2\text{layers}}$  and  $E_{1\text{layer}}$  are the total energy of two montmorillonite layers and the single layer in the supercell, respectively.

An example of the calculations along the [100] sliding path of Na-Mnt is shown in Supplementary Fig. 4 and explained in Supplementary Discussion, DFT Calculations. The interlayer energies  $E_{\text{IL}}$  were calculated every  $\sim 0.5$  Å along the path  $x$  by moving the top layer up and down along the  $z$ -axis. After the movement of the top layer with the displacement of  $L$ , the top layer reaches the crystallographic equivalent positions to the initial positions. In this figure, some stacking structures along the path ( $x = 0, 3/19L, 7/19L, 10/19L$ ) are shown by the overlap of  $\text{SiO}_4$  tetrahedral sheets between the top and bottom layers. The lowest interlayer energy  $E_{\text{IL}}$  is obtained at  $x = 0$ , which corresponds to the stacking structure calculated by the bulk structure optimization. All calculated interlayer energies are shown in Supplementary Fig. 5. The interlayer energies were fitted to an eighth- or seventh-degree polynomial equation. This derivative of the equation was used to estimate the  $z$  position where the interlayer repulsion force balanced the external applied normal force  $f_{\text{ext}}$  as

$$f_{\text{ext}} = -\frac{\partial E_{\text{IL}}(x, z)}{\partial z}. \quad (4)$$

The relative difference in the potential energy is only required for calculating the frictional force; therefore,  $V$  in Eq. 2 was expressed as the difference from the

minimum potential energy in the sliding path. The frictional force  $f_{\text{friction}}$  can be obtained by the derivative with respect to  $x$  of the potential energy  $V$  by

$$f_{\text{friction}}(x; f_{\text{ext}}) = \frac{\partial V}{\partial x}. \quad (5)$$

The shear stress  $\tau_{\text{DFT}}$  was calculated by dividing the friction force by the surface area as shown in Supplementary Fig. 6.

**Density functional theory calculations.** The exchange of interlayer cations will modify the lattice constants of montmorillonite. Therefore, we computed the structure optimization of bulk montmorillonite. The obtained lattice constants were fixed in subsequent slab calculations to estimate the interlayer energy as a function of interlayer distance  $z$  and sliding distance  $x$  along the sliding path. The DFT calculations can provide precise lattice constants and interlayer energy of phyllosilicates<sup>24</sup>. In this method, the exchange and correlation energies were calculated under the generalized gradient approximation of the Perdew-Burke-Ernzerhof (GGA-PBE) method<sup>38</sup>. Only valence electrons in atoms were explicitly considered in the calculations using a pseudopotential method<sup>39</sup>. Weak van der Waals forces were reproduced by a semiempirical dispersion force correction (DFT-D2)<sup>40,41</sup>. All DFT calculations were performed using QUANTUM ESPRESSO<sup>42</sup>. The structures of Mnt were drawn using VESTA<sup>43</sup>.

**Bulk calculations.** A montmorillonite structural model was developed using the muscovite structure as an initial structure by substituting the tetrahedral Al ions to Si ions and partially substituting the octahedral Al ions to Mg ions. Muscovite was chosen because the atomic coordinates and lattice parameters have been determined precisely. There is no influence on the simulations by using muscovite as the basis of montmorillonite because the structure is optimized by the DFT simulations. The supercell includes two layers and 82 ions composed of four (Na or K)<sub>0.5</sub>(Al<sub>1.5</sub>Mg<sub>0.5</sub>)(Si<sub>4</sub>O<sub>10</sub>)(OH)<sub>2</sub> units. The convergence threshold on the stresses was 0.5 kbar. The threshold used to consider the relaxed structure was defined by total ion energies in the supercell ( $<0.0136$  meV) and forces ( $<1.36$  meV bohr<sup>-1</sup> ion<sup>-1</sup>). Kinetic energy cutoffs for wavefunction and charge density were chosen to be 40 Ry (=544.2 eV) and 320 Ry (=4353.6 eV), respectively. These cutoffs were also used for subsequent calculations on slab geometry. Sampling of k-points was established using  $4 \times 2 \times 1$  in Monkhorst-Pack grids<sup>44</sup> in the Brillouin zone.

**Slab calculations.** The area of the shear plane in the supercell was determined from the bulk calculations to be a monoclinic cell of  $a = 10.450$  Å,  $b = 9.049$  Å,  $c = 46.641$  Å, and  $\beta = 87.99^\circ$  for Na-Mnt and  $a = 10.430$  Å,  $b = 9.051$  Å,  $c = 49.178$  Å, and  $\beta = 95.61^\circ$  for K-Mnt. Two Mnt layers were embedded between vacuum regions in the cell by elongating the length  $c$ . Sampling of k-points was set to  $2 \times 2 \times 1$  in Monkhorst-Pack grids. A dipole correction<sup>45</sup> was applied to remove an artifact arising from periodic boundary conditions normal to the basal plane of montmorillonite. Atomic relaxations were conducted for ions in the supercell except for Al and Mg ions in octahedral sites. Fixing the position of these octahedral ions is required to fix the interlayer distance. Atomic relaxations of a single layer in the supercell were also conducted by fixing the position of these octahedral ions.

**Triaxial shear experiments.** Frictional sliding experiments were performed at room temperature on a commercially available Na-montmorillonite, American Colloid Volclay MPS-1, that has the composition Na<sub>0.3</sub>(Fe<sup>2+</sup>, Mg)<sub>0.3</sub>(Al, Fe<sup>3+</sup>)<sub>1.7</sub>Si<sub>4</sub>O<sub>10</sub>(OH)<sub>2</sub>· $n$ H<sub>2</sub>O. This montmorillonite has been tested with distilled water over a wide range of effective normal stress<sup>8</sup>. Na-Mnt samples were tested with 1 molar aqueous NaCl brine as pore fluid. Four other starting materials were prepared by repeated washings of the starting clay with 1M solutions of the appropriate salts (LiCl, KCl, RbCl, and CsCl). In this way, Na was replaced by the corresponding cations at exchange sites. Samples were then sheared with either distilled water (DW) or 1 M<sub>aq</sub> of the corresponding brine pore fluid.

The test procedure, similar to the procedure described in Morrow et al. (2017)<sup>8</sup>, uses a triaxial deformation rig with a cylindrical Berea sandstone sample (76.2 mm-diameter by 190 mm-length) containing a sawcut inclined 30° to the sample axis (Supplementary Fig. 7). A 4 mm thick layer of Mnt clay paste was placed between the sawcut sample halves and inserted into a polyurethane tube (4.8 mm wall thickness) that was sealed to steel endcaps. The sample assembly was placed in a pressure vessel and confining pressure was applied with silicone oil confining fluid. A constant pore pressure of 1.0 MPa was maintained in both high-permeability sandstone driving blocks (Supplementary Fig. 7). Samples were sheared by advancing a piston against the lower steel endcap at alternating rates of 0.01, 0.1, and 1.0 μm/s. A greased Teflon shim between the piston and steel endcap allowed the lateral motion of the lower sample half as slip occurred on the inclined gouge layer. Axial force (measured with an internal load cell) and confining pressure were used to calculate normal stress on the fault surface. Confining pressure was then adjusted under computer control to maintain constant effective normal stress (normal stress minus pore pressure) of 40 MPa. Samples were sheared for approximately 10 mm as shown in Supplementary Material (Supplementary Fig. 8). Wet samples attained nearly constant strength before 1 mm displacement while dry samples required 2–3 mm displacement to reach constant strength. Gouge layers

were compacted by both normal stress and shearing. The initial 4 mm layer thickness was reduced to between 2 and 3 mm when measured after each experiment.

### Data availability

The DFT data that support the findings of this study is available at <https://doi.org/10.17632/3ydkywhs8b.1>. The experimental data that support the findings of this study is available at <https://doi.org/10.5066/P9PB9UXR>.

Received: 9 October 2021; Accepted: 22 April 2022;

Published online: 16 May 2022

### References

- Titus, S. J., DeMets, C. & Tikoff, B. Thirty-five-year creep rates for the creeping segment of the San Andreas fault and the effects of the 2004 Parkfield earthquake: Constraints from alignment arrays, continuous global positioning system, and creepmeters. *Bull. Seismol. Soc. Am.* **96**, S250–S268 (2006).
- Moore, D. E. & Rymer, M. J. Talc-bearing serpentinite and the creeping section of the San Andreas fault. *Nature* **448**, 795–797 (2007).
- Lockner, D. A., Morrow, C., Moore, D. & Hickman, S. Low strength of deep San Andreas fault gouge from SAFOD core. *Nature* **472**, 82–85 (2011).
- Carpenter, B. M., Marone, C. & Saffer, D. M. Weakness of the San Andreas Fault revealed by samples from the active fault zone. *Nat. Geosci.* **4**, 251–254 (2011).
- Ujii, K. et al. Low coseismic shear stress on the Tohoku-Oki megathrust determined from laboratory experiments. *Science* **342**, 1211–1214 (2013).
- Kameda, J. et al. Pelagic smectite as an important factor in tsunamigenic slip along the Japan Trench. *Geology* **43**, 155–158 (2015).
- Ikari, M. J., Saffer, D. M. & Marone, C. Effect of hydration state on the frictional properties of montmorillonite-based fault gouge. *J. Geophys. Res.* **112**, B06423 (2007).
- Morrow, C. A., Moore, D. E. & Lockner, D. A. Frictional Strength of Wet and Dry Montmorillonite. *J. Geophys. Res. Solid Earth* **122**, 3392–3409 (2017).
- Tetsuka, H., Katayama, I., Sakuma, H. & Tamura, K. Effects of humidity and interlayer cations on the frictional strength of montmorillonite. *Earth, Planets Space* **70**, 56 (2018).
- Lockner, D. A., Solum, J. G. & Davatzes, N. The effect of brine composition and concentration on strength of expandable clays. *EOS Trans. AGU* **87**, Fall Meet. Suppl., Abstract T31F-03 (2006).
- Behnsen, J. & Faulkner, D. R. Permeability and frictional strength of cation-exchanged montmorillonite. *J. Geophys. Res. Solid Earth* **118**, 2788–2798 (2013).
- Koster Van Groos, A. F. & Guggenheim, S. The effect of pressure on the dehydration reaction of interlayer water in Na-montmorillonite (SWy-1). *Am. Mineral.* **69**, 872–879 (1984).
- Koster Van Groos, A. F. & Guggenheim, S. Dehydration of K-exchanged montmorillonite at elevated temperatures and pressures. *Clays Clay Miner.* **34**, 281–286 (1986).
- Wu, T.-C., Bassett, W. A., Huang, W.-L., Guggenheim, S. & Koster Van Groos, A. F. Montmorillonite under high H<sub>2</sub>O pressures: Stability of hydrate phases, rehydration hysteresis, and the effect of interlayer cations. *Am. Mineral.* **82**, 69–78 (1997).
- Huang, W.-L., Bassett, W. A. & Wu, T.-C. Dehydration and hydration of montmorillonite at elevated temperatures and pressures monitored using synchrotron radiation. *Am. Mineral.* **79**, 683–691 (1994).
- Israelachvili, J. N. Measurement of the viscosity of liquids in very thin films. *J. Colloid Interface Sci.* **110**, 263–271 (1986).
- Raviv, U., Laurat, P. & Klein, J. Fluidity of water confined to subnanometre films. *Nature* **413**, 51–54 (2001).
- Sakuma, H., Otsuki, K. & Kurihara, K. Viscosity and lubricity of aqueous NaCl solution confined between mica surfaces studied by shear resonance measurement. *Phys. Rev. Lett.* **96**, 046104 (2006).
- Perkin, S., Goldberg, R., Chai, L., Kampf, N. & Klein, J. Dynamic properties of confined hydration layers. *Faraday Discuss.* **141**, 399–413 (2009).
- Karland, O. & Muurinen, A. Bentonite swelling pressure in NaCl solutions - Experimentally determined data and model calculations. *Abstr. Clays Nat. Engineered Barriers Radioact. Waste Confin.* 175–176 (2002).
- den Hartog, S. A. M., Faulkner, D. R. & Spiers, C. J. Low frictional coefficient of phyllosilicate fault gouges and the effect of humidity: Insights from a new microphysical model. *J. Geophys. Res. Solid Earth* **125**, e2019JB018683 (2020).
- Sakuma, H., Kawai, K., Katayama, I. & Suehara, S. What is the origin of macroscopic friction? *Sci. Adv.* **4**, eaav2268 (2018).
- Zhong, W. & Tománek, D. First-principles theory of atomic-scale friction. *Phys. Rev. Lett.* **64**, 3054–3057 (1990).
- Sakuma, H. & Suehara, S. Interlayer bonding energy of layered minerals: Implication for the relationship with friction coefficient. *J. Geophys. Res. B Solid Earth* **120**, 2212–2219 (2015).
- Sakuma, H., Kawai, K. & Kogure, T. Interlayer energy of pyrophyllite: Implications for macroscopic friction. *Am. Mineral.* **105**, 1204–1211 (2020).
- Henkelman, G., Arnaldsson, A. & Jónsson, H. A fast and robust algorithm for Bader decomposition of charge density. *Computational Materials Science* **36**, 354–360 (2006).
- Dieterich, J. H. & Kilgore, B. D. Imaging surface contacts: power law contact distributions and contact stresses in quartz, calcite, glass and acrylic plastic. *Tectonophysics* **256**, 219–239 (1996).
- Abdolhosseini Qomi, M. J., Ebrahimi, D., Bauchy, M., Pellenq, R. & Ulm, F.-J. Methodology for Estimation of Nanoscale Hardness via Atomistic Simulations. *J. Nanomechanics Micromechanics* **7**, 04017011 (2017).
- Sakuma, H. Adhesion energy between mica surfaces: Implications for the frictional coefficient under dry and wet conditions. *J. Geophys. Res. Solid Earth* **118**, 6066–6075 (2013).
- Džidić, I. & Kebarle, P. Hydration of the alkali ions in the gas phase. Enthalpies and entropies of reactions  $M^+(H_2O)_{n-1} + H_2O = M^+(H_2O)_n$ . *J. Phys. Chem.* **74**, 1466–1474 (1970).
- Pashley, R. M. DLVO and hydration forces between mica surfaces in Li<sup>+</sup>, Na<sup>+</sup>, K<sup>+</sup> and Cs<sup>+</sup> electrolyte solutions: A correlation of double-layer and hydration forces with surface cation exchange properties. *J. Colloid Interface Sci.* **83**, 531–546 (1981).
- Moore, D. E. & Lockner, D. A. Crystallographic controls on the frictional behavior of dry and water-saturated sheet structure minerals. *J. Geophys. Res. Solid Earth* **109**, B03401 (2004).
- Kawai, K., Sakuma, H., Katayama, I. & Tamura, K. Frictional characteristics of single and polycrystalline muscovite and influence of fluid chemistry. *J. Geophys. Res. Solid Earth* **120**, 6209–6218 (2015).
- De Pablo, L., Chávez, M. L. & De Pablo, J. J. Stability of Na-, K-, and Ca-montmorillonite at high temperatures and pressures: A Monte Carlo simulation. *Langmuir* **21**, 10874–10884 (2005).
- Perry, E. & Hower, J. Burial diagenesis in Gulf coast pelitic sediments. *Clays and Clay Minerals* **18**, 165–177 (1970).
- Schwarz, U. D. & Hölscher, H. Exploring and explaining friction with the Prandtl-Tomlinson model. *ACS Nano* **10**, 38–41 (2016).
- Okuda, H., Kawai, K. & Sakuma, H. First-principles investigation of frictional characteristics of brucite: An application to its macroscopic frictional characteristics. *J. Geophys. Res. Solid Earth* **124**, 10423–10443 (2019).
- Perdew, J. P., Burke, K. & Ernzerhof, M. Generalized gradient approximation made simple. *Phys. Rev. Lett.* **77**, 3865–3868 (1996).
- Garrity, K. F., Bennett, J. W., Rabe, K. M. & Vanderbilt, D. Pseudopotentials for high-throughput DFT calculations. *Comput. Mater. Sci.* **81**, 446–452 (2014).
- Grimme, S. Semiempirical GGA-type density functional constructed with a long-range dispersion correction. *J. Comput. Chem.* **27**, 1787–1799 (2006).
- Barone, V. et al. Role and effective treatment of dispersive forces in materials: Polyethylene and graphite crystals as test cases. *J. Comput. Chem.* **30**, 934–939 (2009).
- Giannozzi, P. et al. Advanced capabilities for materials modelling with QUANTUM ESPRESSO. *J. PhysicsCondensed Matter* **29**, 465901 (2017).
- Momma, K. & Izumi, F. VESTA 3 for three-dimensional visualization of crystal, volumetric and morphology data. *J. Appl. Crystallogr.* **44**, 1272–1276 (2011).
- Monkhorst, H. J. & Pack, J. D. Special points for Brillouin-zone integrations. *Phys. Rev. B* **13**, 5188–5192 (1976).
- Bengtsson, L. Dipole correction for surface supercell calculations. *Phys. Rev. B* **59**, 12301–12304 (1999).
- Shannon, R. D. & Prewitt, C. T. Effective ionic radii in oxides and fluorides. *Acta Crystallogr. Sect. B Struct. Crystallogr. Cryst. Chem* **25**, 925–946 (1969).
- Tsipursky, S. I. & Drits, V. A. The distribution of octahedral cations in the 2:1 layers of dioctahedral smectites studied by oblique-texture electron diffraction. *Clay Miner.* **19**, 177–193 (1984).

### Acknowledgements

We thank S. Suehara (National Institute for Materials Science, NIMS) for the discussion on the DFT calculations. The DFT calculations were conducted using the Numerical Materials Simulator at NIMS. This work was supported by JSPS KAKENHI Grant Numbers JP20K04115 and JP20H00200 and by the U.S. Geological Survey Earthquake Hazards Program. Any use of trade, firm, or product names is for descriptive purposes only and does not imply endorsement by the U.S. Government.

**Author contributions**

H.S. conducted the simulations and D.L., J.S. and N.C.D. performed the physical experiments. H.S. and D.L. wrote the bulk of the paper.

**Competing interests**

The authors declare no competing interests.

**Additional information**

**Supplementary information** The online version contains supplementary material available at <https://doi.org/10.1038/s43247-022-00444-3>.

**Correspondence** and requests for materials should be addressed to Hiroshi Sakuma or David A. Lockner.

**Peer review information** *Communications Earth & Environment* thanks Raphael Alvim and the other, anonymous, reviewer(s) for their contribution to the peer review of this work. Primary Handling Editor: Joe Aslin.

**Reprints and permission information** is available at <http://www.nature.com/reprints>

**Publisher's note** Springer Nature remains neutral with regard to jurisdictional claims in published maps and institutional affiliations.



**Open Access** This article is licensed under a Creative Commons Attribution 4.0 International License, which permits use, sharing, adaptation, distribution and reproduction in any medium or format, as long as you give appropriate credit to the original author(s) and the source, provide a link to the Creative Commons license, and indicate if changes were made. The images or other third party material in this article are included in the article's Creative Commons license, unless indicated otherwise in a credit line to the material. If material is not included in the article's Creative Commons license and your intended use is not permitted by statutory regulation or exceeds the permitted use, you will need to obtain permission directly from the copyright holder. To view a copy of this license, visit <http://creativecommons.org/licenses/by/4.0/>.

© The Author(s) 2022